All-in-one improvement toward Li_6PS_5Br-Based solid electrolytes triggered by compositional tune

Zhang, Zhixia; Zhang, Long; Yan, Xinlin; Wang, Hongqiang; Liu, Yanyan; Yu, Chuang; Cao, Xiaoting; van Eijck, Lambert; Wen, Bin

DOI
10.1016/j.jpowsour.2018.11.016

Publication date
2019

Document Version
Accepted author manuscript

Published in
Journal of Power Sources

Journal of Power Sources xxx (2018) xxx-xxx

Contents lists available at ScienceDirect

Journal of Power Sources

journal homepage: www.elsevier.com

All-in-one improvement toward Li_6PS_5Br-Based solid electrolytes triggered by compositional tune

Zhixia Zhang[a], Long Zhang[a, *], Xinlin Yan[b], Hongqiang Wang[c], Yanyan Liu[a], Chuang Yu[d], Xiaoting Cao[a], Lambert van Eijck[d], Bin Wen[a]

[a] State Key Laboratory of Metastable Materials Science and Technology, Yanshan University, Qinhuangdao, Hebei, 066004, China
[b] Institute of Solid State Physics, Vienna University of Technology, Wiedner Hauptstr. 8-10, 1040, Vienna, Austria
[c] College of Chemistry & Environmental Science, Hebei University, Baoding, Hebei, 071000, China
[d] Department of Radiation Science and Technology, Delft University of Technology, Mekelweg 15, Delft 2629 JB, the Netherlands

ARTICLE INFO

Keywords:
Li dendrite suppression
Interfacial stability
Argyrodites
Solid electrolytes
All-solid-state batteries

ABSTRACT

Sulfide solid electrolytes possess high ionic conductivity and moderate dendrite suppression capability, but rather poor compatibility against oxide cathodes and metallic Li. Here, we report O-doped Li_6PS_5Br as solid electrolyte synthesized by a facile solid-state sintering. Different from other O-incorporated sulfides, the O atoms in $Li_6PS_{5-x}O_xBr$ prefer to substitute the S atoms at free S^{2-} sites rather than those at the PS_4 tetrahedra. Remarkably, without deteriorating the ionic conductivity, this inorganic solid electrolyte with O doping exhibits comprehensively enhanced properties including excellent dendrite suppression capability, superior electrochemical and chemical stability against Li metal as well as high voltage oxide cathodes, and good air stability. $Li(Ni_{0.8}Co_{0.1}Mn_{0.1})O_2$ and $LiCoO_2$-based all-solid-state batteries with $Li_6PS_{4.7}O_{0.3}Br$ electrolyte deliver high specific capacity, superior rate capability, and outstanding cycling stability accompanied with low interfacial resistivity. This type of inorganic solid electrolytes is promising for all-solid-state batteries with high energy density.

1. Introduction

All-solid-state lithium-ion batteries (ASLIBs) have attracted broad interest for the next generation energy storage system because they overcome the potential safety hazard from volatile/flammable liquid electrolyte and in parallel present several superiorities of high operating voltage, good thermal stability, and easy volumetric miniaturization [1–3]. The major challenges in development of ASLIBs lie in the relative low ionic conductivity of solid electrolyte (SE) and the poor compatibility of SE/electrodes (both cathode and anode) [4–9]. Therefore, apart from the advantages including absence of leakage, high thermal stability, and wide electrochemical windows, it is urgent to develop SEs with good mechanical properties and chemical/electrochemical stability in presence of Li anode and high voltage oxide cathodes, meanwhile maintaining a high ionic conductivity.

Among all promising candidates for ASLIBs, sulfide SEs are especially attractive because of their high ionic conductivity ($\sigma > 0.1\,mS\,cm^{-1}$) and good deformability [10–12]. The merit of the latter makes it easy to assemble all-solid-state batteries with intimate contact on SE/electrode as well as SE/SE powders. Li_6PS_5X (X = Cl, Br, and I) argyrodites as an important family of sulfide SEs possess high ionic conductivity, a wide electrochemical window, wet-chemical processible synthesis, moderate mechanical properties, and low cost raw materials [13–17]. Unlike Li_6PS_5I comprising fully ordered S^{2-} and I^- and Li_6PS_5Cl comprising fully disordered S^{2-} and Cl^-, Li_6PS_5Br (LPSB) comprises a mixture of ordered and disordered structures, thus demonstrating the fastest Li^+ mobility in the Li_6PS_5X family [18].

Despite of these advantages, the theoretical study indicates a small electrochemical stability window in Li_6PS_5X as in other sulfides [19], which indicates that this type of SEs is easy to be oxidized at high voltages and reduced at low voltages. Oxidative degradation of Li_6PS_5Cl upon cycling by high voltage oxide cathode ($LiCoO_2$, $LiNi_{1/3}Co_{1/3}Mn_{1/3}O_2$, and $LiMn_2O_4$.) is experimentally reported with the resultants of elemental sulfur, sulfides, phosphates, and LiCl [20,21]. In addition, other issues commonly existed in sulfides also lead to the failure or capacity fading in Li_6PS_5X-based ASLIBs, e.g., space-charge layer and ele-

* Corresponding author.
Email address: lzhang@ysu.edu.cn (L. Zhang)

https://doi.org/10.1016/j.jpowsour.2018.11.016
Received 5 August 2018; Received in revised form 31 October 2018; Accepted 5 November 2018
Available online xxx
0378-7753/

mental mutual diffusion at the interface of SE/oxide cathode [4,9,22–26]. Interfacial resistance and stability affected by these issues crucially determine the electrochemical properties and cycle life in a battery. An usual and effective way to mitigate interfacial reaction is to form a protective oxide coating layer on the surface of oxide active materials [4]. Meanwhile, to develop new SEs possessing the capability to form self-limiting interface is proposed to manipulate the long-term interfacial stability [1,5].

On the other hand, regarding the metallic Li negative electrode, Li_6PS_5X is chemical/electrochemical unstable against Li metal and decomposed to LiX, Li_2S, and Li_3P by contacting [27,28]. Moreover, Li dendrites quickly form in the sulfide electrolytes at the current density ~0.4 mA cm^{-2} tested on a Li/SE symmetric cell [29,30]. Considering Li metal as the most promising anode due to its low electrode potential and atomic weight, it is essential to improve the dendrite suppression capability and the compatibility toward metallic Li for Li_6PS_5X. Various methods have thus been proposed as follows: high shear modulus along with good stiffness, fast ion transport, microstructural optimization, usage of additive or buffer/artificial layers, and formation of a passivating layer [9].

Apart from the external coating and/or modification, an internal way via compositional tune to solve above-mentioned interfacial issues is very attractive because an improvement of SE itself allows further battery-level optimization through combining diverse external methods. To the best of our knowledge, however, very few study has been reported so far for sulfide SEs on Li dendrite suppression by compositional tune [29,31,32]. For the stability of SE/electrodes, oxygen incorporation in sulfide SEs has been reported to partially solve the interfacial issues. For example, Li_2O in Li_2S—P_2S_5 inhibits mutual diffusion [33]; O-doped $Li_{10}GeP_2S_{12}$ [34] $75Li_2S$—$24P_2S_5$—$1P_2O_5$ [35], and Li_3PO_4-doped $Li_7P_3S_{11}$ [36] increase the stability against oxide cathodes; LiAlSO [37] and $Li_{3+5u}P_{1-u}S_{4-v}O_v$ [38] improve the stability against Li metal. Nevertheless, it is still not clear whether O doping can simultaneously improve the interfacial stability on both oxide and Li electrodes. Moreover, O doping improves the elastic modulus [39,40] and O-contained reduced interphases may be favorable to form a self-limiting interface with a broad electrochemical window [8,19,37,41]. Another benefit of O substitution for S atoms is to reduce the moisture sensitivity of sulfides [42]. It is thus highly motivated to introduce O in Li_6PS_5X to clarify the interfacial behavior on both electrodes and its effect on Li dendrite suppression.

We herein demonstrate the strong correlation of O incorporation with the interfacial performance at both electrodes as well as Li dendrite formation in LPSB SEs. The intensively enhanced dendrite suppression capability was revealed by Li plating-stripping cycling tests at high operating current densities. A systematical study on interfacial characterization confirmed the superiority of O doping simultaneously on electrochemical/chemical compatibilities of electrolyte against $Li(Ni_{0.8}Co_{0.1}Mn_{0.1})O_2$ (NCM-811) and Li metal electrodes, which possess great potential applied in electric vehicles [9]. The conductive additive was not added to avoid its influence on the interface during electrochemical processes [43], because carbon was found to promote decomposition of sulfide solid electrolytes and NCM-811 delivers relatively high electronic conductivity. The significant improvement on all aspects of O-doped LPSB SE enables corresponding all-solid-state batteries to achieve high specific capacity, good Coulombic efficiency, as well as excellent rate and cycling performance. A carful compositional tune can still be a powerful way to acquire a superior SE [44].

2. Experimental section

2.1. Theoretical study of $Li_6PS_{4.7}O_{0.3}Br$

First-principles calculations based on DFT were performed by using the Vienna *ab initio* simulation package (VASP). The exchange-correlation energy was treated within the generalized gradient approximation (GGA), using the Perdew-Burke-Ernzerhof (PBE) functional relationship. The kinetic energy cutoff of 300 eV was used. All structures were optimized using the conjugate gradient method, the energy convergence value between two consecutive steps was chosen as 10^{-6} eV, a maximum force of 10^{-2} eV $Å^{-1}$ was allowed on each atom. For cell relaxation calculations, the Brillouin zone was sampled using a $2 \times 2 \times 2$ Monkhorst-Pack *k*-point scheme.

2.2. Sample preparation

$Li_6PS_{5-x}O_xBr$ ($0 \leq x \leq 1$) compounds were prepared using solid-state sintering. The starting anhydrous materials Li_2S (Alfa Aesar, 99.9%), P_2S_5 (Alfa Aesar, 99.9%), LiBr (Alfa Aesar, 99.9%), and Li_2O (Alfa Aesar, 99.9%) were weighted in the appropriate stoichiometric ratio and well mixed in an agate mortar. The mixtures were loaded into glassy carbon crucibles, sealed under vacuum in quartz tubes, slowly heated to 600 °C at 0.3 °C/min to avoid extensive exothermal reactions, dwelled for 48 h followed by cooling down naturally in the furnace. The resultant ingots were ground in an agate mortar for further uses. All procedures except quartz sealing were carried out in an argon-filled glove box (H_2O, $O_2 < 0.5$ ppm).

2.3. Structural characterization

XRD was performed using a Rigaku D/MAX/2500/PC (Cu K_α, 40 kV 200 mA). The specimens were loaded to holders in a glove box with Ar atmosphere and then sealed using Kapton films to prevent hydrolysis. Rietveld refinements were performed using the FULLPROF program to determine the lattice parameter [45]. The air stability measurements were carried out in air with a relative humidity of ~35%. Morphological characterizations were performed using a SEM (Hitachi S-4800 II FESEM) equipped with an EDS instrument. Raman scattering measurements were performed using a Renishaw inVia system with a 532 nm excitation source. DSC and TG profiles were recorded on a Perkin-Elmer DSC8000 with a scan rate of 10 °C/min.

2.4. Electrochemical characterization

EIS measurements were performed in the frequency range from 0.1 Hz to 3 MHz at ambient temperature with an impedance analyer (Princeton P4000). Heating scans from room temperature to 90 °C were performed to determine the temperature dependence of the ionic conductivity. The pellets for measurements were cold-pressed from powders at approximately 400 MPa with indium foils placed on both sides of the pellets. The sandwiched pellets were then mounted on an air-tight two-electrode cell with two stainless-steel rods as current collectors. The CV measurements were carried out in the voltages range of −0.5 V to 10 V at a scan rate of 0.05 mV s^{-1} on SS/LPSOB-0.3 (LPSB)/Li cells, where SS is working electrode and Li is counter/reference electrode. To evaluate the compatibility of LPSOB-0.3 (LPSB) toward metallic Li, Li plating-stripping galvanostatic cycling tests were performed on Li/LPSOB-0.3 (LPSB)/Li symmetric cells at different current densities on a LAND cell test instrument. DC polarization test was performed to determine the electronic conductivity of the composite electrode using Princeton 4000. The ion-blocking SS/composite electrode/

SS cell was assembled by placing SS foils on the two sides of cold-pressed composite electrode pellet.

2.5. Fabrication of all-solid-state battery

Laboratory-scale all-solid-state NCM-811 ($LiCoO_2$)/LPSOB-0.3 (LPSB)/Li—In (Li) cells were constructed by employing NCM-811 ($LiCoO_2$) active material in combination with LPSOB-0.3 (LPSB) as positive electrode, together with Li—In (Li) negative electrode and LPSOB-0.3 (LPSB) as SE. For positive electrodes, the NCM-811 ($LiCoO_2$) commercial powders were mixed with LPSOB-0.3 (LPSB) electrolytes in a volume ratio of 1:1 by hand ground for 0.5 h. Bilayer pellets comprising the composite positive electrodes (15 mg) and LPSOB-0.3 (LPSB) electrolytes (125 mg) were obtained by cold pressing under 300 MPa. Li—In (Li) foil was then attached to the SE side of the bilayer pellets by pressing under 20 MPa. Finally, the three-layer pellet was then sandwiched between two stainless steel rods acted as current collectors. All processed were performed in an Ar-filled glove box. Electrochemical properties of all-solid-state batteries were investigated by galvanostatic charge-discharge tests at different C rate on a LAND system under a cut-off voltage of 2 V–3.7 V (*versus* Li—In). The specific capacity was calculated based on the mass of the active material. The EIS measurements of the cells were carried out on a Princeton P4000 workstation from 0.01 Hz to 3 MHz by applying a potential of 10 mV.

2.6. Electronic supplementary information (ESI) available

Morphology, EDX mapping, XRD, XRD profiles before and after air exposure, voltage curves for Galvanostatic intermittent cycling, Nyquist plots of Li/electrolyte symmetric cells and the equivalent circuit fitting, DSC curves of the mixture of Li/SEs, cycling performance of NCM-811/Li cells, discharge capacity of NCM-811/Li—In cells with different batches of SEs, electrochemical performance of $LiCoO_2$/Li—In cells.

3. Results and discussion

3.1. Structural properties of $Li_6PS_{5-x}O_xBr$

Fig. 1a shows the XRD patterns of the synthesized $Li_6PS_{5-x}O_xBr$ ($0 \le x \le 1$). All samples are dominated with the argyrodite phase. The samples with $0 \le x \le 0.2$ are single phase. Further increasing O concentration, a slight amount of impurities indexed by Li_3PO_4 when $x \ge 0.25$ and indexed by LiBr when $x \ge 0.6$ are observed. The lattice parameter a ($a = b = c$) (Fig. 1b) of the argyrodite phase shows a nonlinear dependence with x. It decreases at the beginning, reaches a minimum value of 9.9695 Å ($x = 0.2$), and then increases with increasing x until reaches a saturation of ~10 Å when $x > 0.3$. The substitution of O at the S sites contributes to the reduction of the lattice parameter when $x < 0.2$ because of the smaller ionic radius of oxygen in contrast to that of sulfur [34]. The increase of lattice parameter for $x \ge 0.25$ is speculated as a consequence of formation of interstitial atoms from O and/or off-stoichiometric ratio due to the impurity phase [34]. The competition of lattice contraction and expansion reaches a balance or a solubility limit is reached for $x > 0.3$, thus maintaining a constant value of the lattice parameter. The morphology (Fig. S1) of the O-doped sample is basically the same as that of the pristine sample, both displaying a flower-like lamellar shape. This could be happen because the shape of final samples depends on lots of factors such as the crystal growth preferences and synthesis conditions. The energy dispersive spectrometry (EDS) mapping (Fig. S2) of the selected sample $Li_6PS_{4.7}O_{0.3}Br$ (LPSOB-0.3) demonstrates homogeneous distribution of each element (S, P, O, Br).

As it is basically difficult to locate O atoms in the structure due to the small quantity, we performed first-principles calculations based on density functional theory (DFT) to understand the thermodynamic stability of O doping. Three models regarding various S positions were adopted for geometrical optimization, corresponding to S1 at 16*e*, S2 at 4*d*, and S3 at 4*a* site. When the S1 site was partially replaced by O atoms, the structural symmetry totally changed; the total energy couldn't converge to a stable value; and the atomic positions became disordered. This indicates that the obtained structure by partially doping O on the S1 position is not stable or not existing. On the contrary, when the S2 or S3 site was substituted by O atoms, the total energy reaches a stable value of −4432.84 and −4454.19 eV, respectively, and the space group of F-43 m is maintained as pristine LPSB. Therefore, the introduced O atoms would prefer to occupy the 4*a* and/or 4*d* sites. Fig. S3 depicts the schematic framework of O-doped LPSB based on this viewpoint.

The influence of O substitution on the chemical structure is further understood from Raman spectra. All observed peaks (Fig. 1d) at 275, 421, 571, and 594 cm^{-1} can be assigned to the PS_4^{3-} tetrahedral anion. The position of the typical characteristic peak at 421 cm^{-1}, assigned to

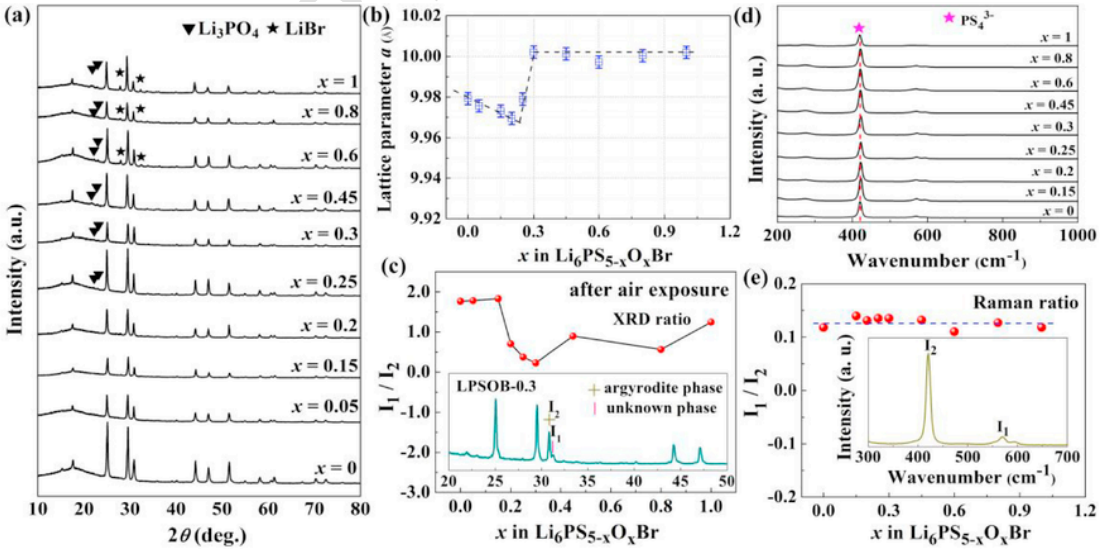

Fig. 1. (a) XRD patterns of $Li_6PS_{5-x}O_xBr$ ($0 \le x \le 1$). (b) Compositional dependence of the lattice parameter for $Li_6PS_{5-x}O_xBr$. (c) Intensity ratio of the impurity to the argyrodite phase after $Li_6PS_{5-x}O_xBr$ exposed in air for 10 min. (d) Raman spectra of $Li_6PS_{5-x}O_xBr$ ($0 \le x \le 1$). (e) The intensity ratio of I_1/I_2 as a function of x in Raman spectra.

A_1 symmetric stretching vibration of the PS_4^{3-} tetrahedral anion [46], keeps unchanged regardless of O concentration. Fig. 1e shows the Raman relative intensities of I_1/I_2, where I_1 represents the characteristic peaks at 571 cm^{-1} related to internal stretching vibrations. The ratio remains nearly constant with increasing O concentration. It has been reported that a slightly shorter bond can cause the blue shift of the wavenumber in Raman spectrum [47], and slight O doping on PS_4 leads to a significant change of Raman characterization [34,36]. Therefore, the identical Raman spectra in $Li_6PS_{5-x}O_xBr$ system indicates that O doping neither changes the local structure of PS_4^{3-} group nor forms a new anion group. This result indicates that O atoms do not substitute S atoms at the S1 (16*e*) site, in good agreement with XRD and theoretical calculation results.

As partial substitution of O on S is expected to suppress the hydrolysis of sulfide SEs in the humid environment, chemical stability of $Li_6PS_{5-x}O_xBr$ was evaluated using XRD after exposure to air with ~35% relative humidity. The impurity phases (Fig. S4) appear after exposing the samples in air for 10 min. Fig. 1c displays the intensity ratio of the impurity to the argyrodite phase (at $2\theta \approx 31^\circ$) as a function of O concentration. A low doping concentration ($x < 0.2$) shows negligible influence on hydrolysis suppression. When $x \geq 0.2$, the intensity ratio is rapidly reduced by 2/3 and gradually decreases to a minimum value for $x = 0.3$, and then slightly increases when $x \geq 0.45$. Oxygen doping obviously improves the air stability of LPSB, in accordance with the results reported previously [42,48,49].

3.2. Electrochemical performance of $Li_6PS_{5-x}O_xBr$

Understanding the DC cycling performance against a short circuit induced by Li dendrite is important because the working current density approaching 1 mA cm^{-2} is relevant to vehicle electrification [30]. The dendrite suppression capability of $Li_6PS_{5-x}O_xBr$ SEs was evaluated by galvanostatic intermittent cycling of Li/$Li_6PS_{5-x}O_xBr$/Li symmetric cells with step-increased current density at 25 °C. The voltage-time plots as a function of current density for $x = 0$ and 0.3 are respectively illustrated in Fig. 2a and b, and those for the other O concentrations are illustrated in Fig. S5. The polarization voltage for all measured samples increases with increasing current. The pristine sample shows a higher initial voltage than O-doped samples. For example, the value is 0.0114 V for $x = 0$ (Fig. 2a) whereas is 0.0057 V for $x = 0.3$ (Fig. 2b). Considering the comparable ionic conductivity of these two samples (Fig. 3a, see below), a larger initial voltage could be induced by higher interfacial resistance. This indicates that O doping improves the chemical/electrochemical stability of electrolyte to metallic Li. With increasing current density, the voltage sharply drops near to zero at a certain current density, indicating a short circuit inside the SE induced by penetration of Li dendrite propagated [30,50]. The critical current density, defined as the current segment value where the voltage drop occurred, is adopted to evaluate the dendrite suppression capability in an electrolyte, as illustrated in Fig. 2c. The critical current density of O-free LPSB is 0.45 mA cm^{-2}, comparable to that of $75Li_2S—25P_2S_5$ (0.5 mA cm^{-2}) [30], whereas the value significantly increases with O doping. The samples with moderate O concentrations ($0.3 \leq x \leq 0.6$) possess excellent dendrite suppression capability and demonstrate critical current density values close to 0.9 mA cm^{-2}, comparable to hot-pressed $75Li_2S—25P_2S_5$ [30] and LiI-incorporated $75Li_2S—25P_2S_5$ [29]. The reason for the decrease of critical current density when $x > 0.3$ still needs further investigation, however, it may be attributed to the increased impurities by higher O doping concentrations (Fig. S4) [29]. The critical current density is supposed to be further improved by hot pressing or LiI incorporation. We further compare the long time Li plating/stripping reversibility using the Li—Li symmetric cells with and without O-doped electrolyte. As shown in Fig. 2d, at a low current density of 0.1 mA cm^{-2}, LPSB can sustain 560 cycles before a short circuit (the inset of Fig. 2d), while LPSOB-0.3 can perfectly work over 900 cycles at a higher current density of 0.4 mA cm^{-2}. In addition, the corresponding voltage are extremely stable during cycling, indicating that a stable interfacial layer is formed in the initial cycle. The ex situ scanning electron microscope (SEM) cross-section images further confirm the important role of O on the dendrite suppression. Plenty of cracks

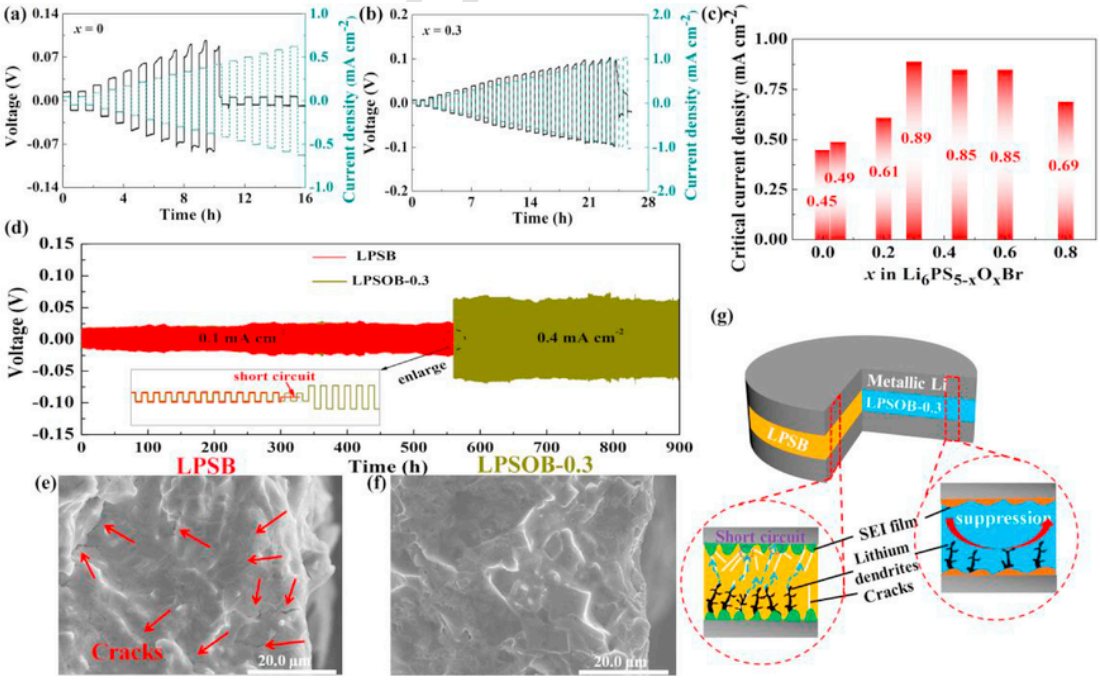

Fig. 2. Galvanostatic intermittent cycling of the Li/$Li_6PS_{5-x}O_xBr$ symmetric cells for (a) $x = 0$ and (b) 0.3 at step-increased current density at 25 °C. (c) The critical current density of $Li_6PS_{5-x}O_xBr$ ($0 \leq x \leq 1$). (d) Galvanostatic cycling of the Li/LPSB and Li/LPSOB-0.3 symmetric cells at constant current densities of 0.1 mA cm^{-2} and 0.4 mA cm^{-2}. The cross-sectional SEM images at the interface of electrolyte/Li for (e) $x = 0$ after short circuit and (f) $x = 0.3$ after 900th cycle. (g) Schematic diagram illustrating the excellent dendrite suppression capability for LPSOB-0.3 in contrast to LPSB.

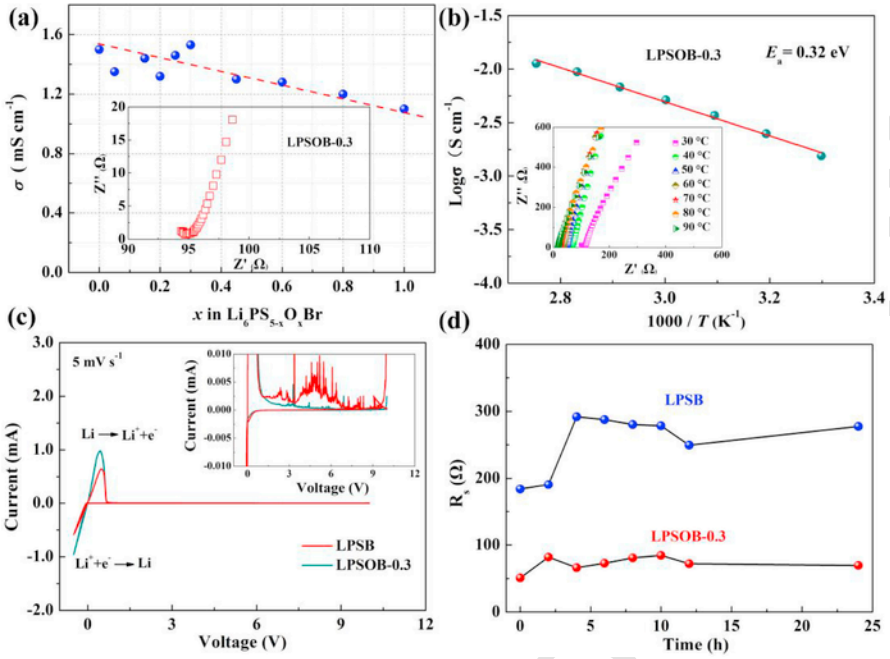

Fig. 3. (a) Composition dependent room temperature ionic conductivity for $Li_6PS_{5-x}O_xBr$ ($0 \le x \le 1$). (b) Arrhenius conductivity plot of LPSOB-0.3 from 30 °C to 90 °C. Inset displays the corresponding impedance spectrum. (c) Cyclic voltammograms of LPSB and LPSOB-0.3 electrolytes. Inset shows the magnified CV curves in the current range of −0.01 mA to 0.01 mA. (d) Time dependent interfacial resistance for LPSB and LPSOB-0.3 electrolytes after contacting with Li.

are apparently observed in LPSB SE after 560 cycles (Fig. 2e) whereas LPSOB-0.3 after 900 cycles (Fig. 2f) is still perfect, indicating an excellent dendrite suppression capability via O doping.

With the prerequisites of the comparable ionic conductivity (Fig. 3a) and microstructural integrity (Fig. S1), as well as the same cell assembling processes, we proposed that the mechanism for the enhanced dendrite suppression capability of LPSOB-0.3 in comparison with pristine LPSB lies on the strengthened shear modulus and the O-contained interfacial layer, as depicted in Fig. 2g. Previous studies reveal that Li dendrite suppression capability is relevant to the shear modulus of the electrolyte [40,51]. Oxides normally show higher elastic modulus (both Young's modulus and shear modulus) than sulfides [39,52]. Higher elastic modulus is also found in O-doped sulfides. For example, the Young's modulus increases with P_2O_5 doping concentration in $70Li_2S{\cdot}(30\text{-}z)P_2S_5{\cdot}zP_2O_5$ system [40]. Hence, the shear modulus of LPSOB-0.3 would be higher than that of LPSB, which is beneficial to suppress the growth of Li dendrite. In parallel, the interfacial layer plays an important role for dendrite suppression [29]. In contact with metallic Li, Li_6PS_5X argyrodites were found to decompose into interphases composed of Li_3P, Li_2S and LiX, resulting in an enlarged interfacial resistance [27]. In view of this point, the additional decomposed phase of LPSOB-0.3 compared with LPSB should be one or more O-contained interphases. At least, the formation of Li_3OBr is confirmed from the XRD measurement (Fig. S6) on the Li plate detached from the Li/LPSOB-0.3/Li cell after cycling tests. Li_3OBr has been reported previously as a superionic conductor with 3-dimensional Li^+ migrating channels [53]. Therefore, the formation of Li_3OBr improves the ionic conductivity of the interface at electrolyte/Li and increases the mobility of Li atoms [29]. This is favorable for the Li deposition at the interface and thus suppressing the dendrite growth. In addition, thin interfacial layer with oxide may be favorable to dendrite suppression because of its high chemical stability and capability to restrain the breakage and repair of the interfacial layer during the Li plating/stripping process [54]. Accordingly, the enhanced shear modulus of the SE coupled with oxide-contained interfacial layer (e.g. Li_3OBr) for O-doped LPSB enables the excellent dendrite suppression capability.

The ionic conductivity of $Li_6PS_{5-x}O_xBr$ was evaluated by the AC impedance method at room temperature. A typical impedance spectrum of $Li_6PS_{5-x}O_xBr$ (inset of Fig. 3a) contains a fraction of semicircle in the high-frequency region associated with a negligible grain boundary resistance, followed by a linear steep spike in the low-frequency regions associated with the capacitive behavior similar to the blocking electrodes. This means that $Li_6PS_{5-x}O_xBr$ SEs are typical ionic conductors with an overall resistance dominated by the bulk component, which is expected for sulfide ion conductors. Fig. 3a shows the room temperature ionic conductivity (σ) of $Li_6PS_{5-x}O_xBr$ calculated from the total resistance. The ionic conductivity shows a slightly decreasing dependence with O doping, which could be attributed to the slight contraction of the unit cell by O doping, strong electrostatic attraction between O and Li ions, and gradually increased impurity phases [34,36,38]. Nevertheless, all samples show σ over 1.1 mS cm^{-1}, especially for samples where $x \le 0.3$ possessing values around 1.4 mS cm^{-1}. The ionic conductivity of $Li_6PS_{5-x}O_xBr$ is several orders of magnitude higher than that of Li_6PO_5Br ($\sim 10^{-6}$ mS cm^{-1}) reported previously [55]. High ionic conductivity is favorable for a good battery performance. Although the impurities appear for samples where $x > 0.2$, LPSOB-0.3 was selected for further investigation because of high ionic conductivity, good air stability, and more important, excellent dendrite suppression capability.

Fig. 3b shows the reciprocal temperature dependence of the ionic conductivity of LPSOB-0.3. The linear dependence of logσ *versus* ($1/T$) obeys the Arrhenius law, confirming a good thermal stability of LPSOB-0.3 over the measured temperature range [14]. The ionic conductivity increases from 1.54 mS cm^{-1} at room temperature to 11.32 mS cm^{-1} at 90 °C, approaching to those of organic liquid electrolytes currently used at room temperature [11]. The activation energy E_a for Li^+ conduction was determined from the slope of the linear Arrhenius plot using the equation: $\sigma = A \exp(-E_a/k_BT)$, where A is the pre-exponential parameter and k_B is the Boltzmann constant. The calculated activation energy of LPSB-0.3 is 0.32 eV and comparable to those of Li_6PS_5X argyrodites [14,15,56].

Fig. 3c displays the cyclic voltammograms of $Li_6PS_{5-x}O_xBr$ ($x = 0$, 0.3) swept between −0.5 V to 10 V *versus* Li/Li^+ with the electrolyte

sandwiched between stainless steel (SS) and Li electrodes. A larger responding current is observed in LPSOB-0.3 in comparison with LPSB, which is attributed to the smaller interfacial resistance in SS/LPSOB-0.3/Li cell. This indicates a more stable interface in LPSOB-0.3/Li than LPSB/Li. It is notable that, when magnified the cyclic voltammetry (CV) curves in the current range from −0.01 mA to 0.01 mA (inset of Fig. 3c), several broad peaks with currents of 3–7 μA appear for LPSB-based cell during the anodic scan whereas a smooth curve without reaction is observed for LPSOB-0.3-based cell. This result further confirms that O doping improves the electrochemical stability of $Li_6PS_{5-x}O_xBr$ SEs, which agrees with previous results shown in other sulfides [57,58].

As indicated by galvanostatic cycling tests on Li symmetric cells and the CV measurements afore-mentioned, O-doped electrolyte possesses a lower interfacial resistance than O-free electrolyte. It has been reported that the interfacial layer of SE/Li grows with time, which causes the increase of interfacial resistance [27]. Time-resolved electrochemical impedance spectroscopy (EIS) measurements were thus performed to compare the interfacial resistance of O-doped and pristine samples. Nyquist plots of Li/LPSB (LPSOB-0.3)/Li cell as a function of contacting time were displayed in Fig. S7. The spectra contain two semicircles associated with the interfacial resistance in the high frequency regions and the charge transfer process in the low frequency regions [59]. As shown in Fig. S8, the equivalent circuit $R_b(R_sQ_s)$ ($R_{ct}Q_{ct}$) was used to fit the obtained impedance data, where R_b represents the resistance of the electrolyte corresponding to the high frequency intercept at the real axis, the parallel combination of (R_sQ_s) represents the contribution of interface, and ($R_{ct}Q_{ct}$) is used to describe the charge transfer resistance. Fig. 3d shows the obtained interfacial resistance (R_s) for LPSB and LPSOB-0.3 SEs. R_s of LPSB sharply increases after 2 h contacting, indicating a severe decomposition of LPSB with metallic Li. In contrast, the interfacial resistance of LPSOB-0.3 only slightly increases. It is worth to be noted that both the initial and the aged interfacial resistances of LPSOB-0.3 are almost four times lower than those of LPSB. These results confirm that incorporation of oxygen in LPSB not only enhances the long term chemical stability of SE/Li but also reduces the interfacial resistance of SE/Li, in good agreement with the galvanostatic cycling and CV results. This can be understood by 1) well contacted interfacial layer of electrolyte/Li for O-doped electrolyte and 2) O-contained interfacial layer mitigating further decomposition of electrolyte [38]. The interface between Li and electrolyte can be distinguished with its physical properties by three different types including [60,61]: 1) a thermodynamically stable interface, 2) a mixed conducting and reactive interface, and 3) a reactive but kinetically stabilized interphase with electron- and/or ion-blocking properties. Since the interfacial resistance is nearly stable after 4 h of contact, the type of interphase formed in LPSB/Li and LPSOB-0.3/Li belong to the 3rd one, i.e., a stable interface has formed, similar to that of $Li_7P_3S_{11}$ [61].

The reactiveness of LPSB and LPSOB-0.3 with metallic Li were further investigated through differential scanning calorimetry (DSC) and thermogravimetric (TG) measurements. DSC curves (Fig. S9) for the two samples are very different. Reversible endothermic and exothermic peaks appear at ~180 °C, corresponding to Li melt and solidification. The 1st and 2nd thermal cycles of LPSB do not overlap and appear strong fluctuations after heating over 180 °C, which could be attributed to the strong chemical reaction between LPSB and Li after melting [62]. The resultants are all solid phases because no weight loss is detected from the TG curve (Fig. S9c) for both samples. Moreover, the exothermic peak is missing for LPSB at the 2nd cycle, indicating no solidification during cooling. This we interpret as a consequence of the complete reaction between LPSB and melted Li. In contrast, the two cycles of LPSOB-0.3 are well overlapped except the small fluctuation appeared in the 1st cycle. We thus conclude that the incorporation of oxygen significantly enhances the chemical compatibility of LPSB against metallic Li.

3.3. All-solid-state NCM-811 and $LiCoO_2$ batteries

Cell performance is not only dependent on the ionic conductivity of SE but also on the interfacial stability [33]. All-solid-state batteries based on NCM-811 positive electrode and Li—In negative electrode were set up to evaluate the compatibility of SE toward oxide cathode. The cross-sectional SEM images (Fig. S10) show relatively good contact between NCM-811 and LPSOB-0.3 in the positive electrode. No electronic conductor was used at the positive electrode to avoid the influence of electronic additive on sulfide. The electronic conductivity of the composite cathode was calculated to be 1×10^{-6} S/cm with DC polarization method (Fig. S11). Fig. 4a shows the initial charge–discharge voltage profiles of NCM-811/Li—In cells using LPSB and LPSOB-0.3 SEs. Both cells show a poor columbic efficiency (η) at the first cycle, especially for that using LPSB electrolyte with a columbic efficiency as low as 16%. This huge capacity loss can be attributed to severe side effects including [4,20,63,64]: 1) chemical diffusion between active material and electrolyte, 2) consumption of active materials, and 3) formation of a space-charge layer due to a large chemical potential difference and different conducting type between oxide cathode and electrolyte. In contrast, the cell using LPSOB-0.3 electrolyte achieves a reversible discharge capacity of 106 mAh g^{-1} and a columbic efficiency of 47%, which are over 3 times higher than that using O-free LPSB. Mechanism for mitigating the side effects by O doping (Fig. 4b) is proposed as follows. First, oxygen substitution for sulfur in LPSOB-0.3 limits the chemical diffusion of cathode/electrolyte [33]. Second, O atoms in LPSOB-0.3 inhibit the consumption of the active material by the electrolyte upon delithiation because of the larger electronegativity of oxygen than that of sulfur [63]. Third, the confined space-charge layer for O-doped electrolyte [4,10]. Based on the theory of space-charge layer, Li^+ is likely to transfer from LPSB to NCM-811 during the formation of the space-charge layer due to the strong binding energy of Li—O than that of Li—S. NCM-811 should thus accommodate extra Li^+, which are deintercalated in the beginning of the 1st charging. This deintercalation process gives an extra oxidative steps presenting as a slope, which can be adopted to evaluate the degree of the space-charge layer [65]. Compared the slope shown in Fig. 4a, the contribution of the space-charge layer for LPSB and LPSOB-0.3 cells locates in the voltage range of 2.2 V–3.2 V and 2.2 V−3.0 V, respectively, leading to a capacity of 145 and 63 mAh g^{-1}. The capacity difference induced by space-charge layer is 82 mAh g^{-1}, indicating an intensively suppressed space-charge layer by O doping. From these viewpoints, we can conclude that incorporation of oxygen in LPSB reduces the side reaction of oxide cathode/electrolyte through all three ways, especially space-charge layer, to maintain a low interfacial resistance as well as to avoid degradation of SE. The initial capacity loss might be further mitigated by: 1) stabilizing the chemical potential difference via surface coating with electronically insulating and ionically conducting oxides or inclusion of sulfides in electrolytes; 2) doping cathode with cations such as Cr—, Fe— and Ga; 3) using smaller particle size of cathode materials in the composite electrode; 4) inserting a buffer layer inside cathode/electrolyte or designing multilayer/sandwich electrolyte.

The advantage of LPSOB-0.3 is also reflected in the rate capability. Fig. 4c and d show the charge–discharge curves of the NCM-811/Li—In batteries with LPSOB-0.3 and LPSB electrolytes under various current densities, respectively. The charge–discharge rates vary from 0.1 C to 0.8 C, corresponding to current densities of 0.214 mA cm^{-2} to 1.712 mA cm^{-2}. The discharge capacity decreases from 108.7 mAh g^{-1} at 0.1 C to 47.4 mAh g^{-1} at 0.8 C for the cell with LPSOB-0.3, whereas the discharge capacity is as low as 32.3 mAh g^{-1} at 0.1 C and decreases near to zero at 0.8 C for the cell with LPSB. The cell with pristine LPSB

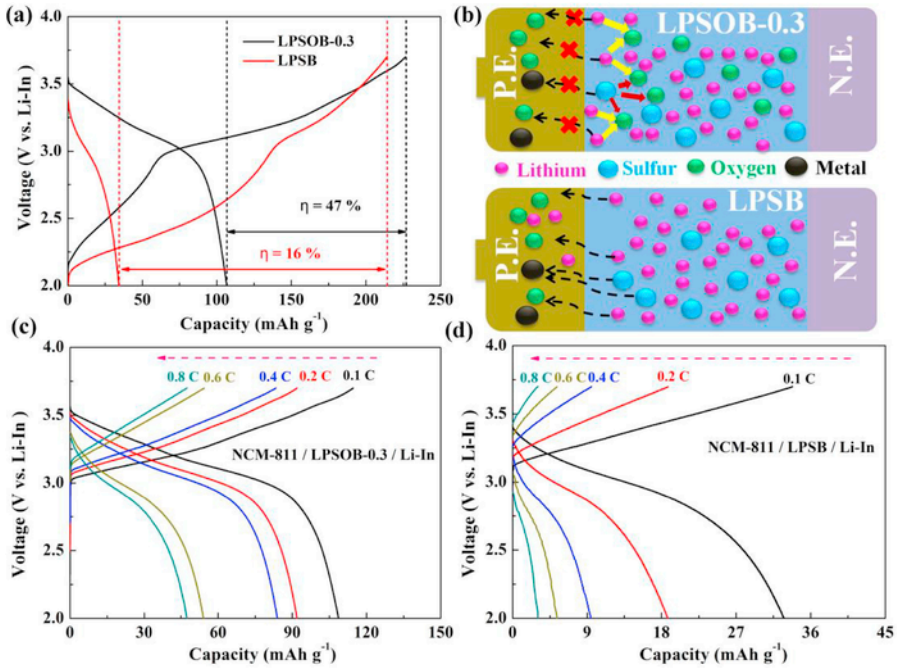

Fig. 4. (a) The initial charge–discharge curves of NCM-811/LPSOB-0.3/Li—In and NCM-811/LPSB/Li—In cells. (b) Schematic illustration of the advantage of O incorporation. Representative charge–discharge profiles of (c) NCM-811/LPSOB-0.3/Li—In and (d) NCM-811/LPSB/Li—In cells at different current densities.

shows very poor rate capability as the capacity is almost cut in half from 0.1 C to 0.2 C accompanied with an increased polarization.

Cycling performance of all-solid-state NCM-811 cells with pure metallic Li as negative electrode was also investigated, as shown in Fig. S12. The cell with LPSOB-0.3 electrolyte can well run with a stable discharge capacity of 35 mAh g^{-1} over 92 cycles without a short circuit, whereas the cell with LPSB electrolyte can only run for 1 cycle and then the short circuit occurs during the 2nd charging process. Both cells show a large polarization and severe capacity loss in the 1st cycle, indicating that a higher O doping concentration is required for further inhibiting the decomposition of SE at the anode site. This capacity fading is ascribed to the increased interfacial resistance because the low redox potential of Li anode leads to formation of a thick interfacial layer at the Li anode/SE interface [34]. Nevertheless, this result further confirms that O doping significantly enhances the dendrite suppression capability and the electrochemical stability of LPSB against metallic Li.

Cycling performance at different current densities for NCM-811/Li—In cells with LPSOB-0.3 and LPSB SEs are respectively shown in Fig. 5a (the first 35 cycles were magnified in the inset) and 5b. Both cells demonstrate good cycling stability at each rate step from 0.1 to 0.8 C and excellent reversibility with a Coulombic efficiency approaching 100% after few cycles, indicating a facile Li^+ insertion-extraction process. The recoverable capacity is nearly 100% when the current density turns back to 0.1 C. The cycling stability of NCM-811 together with LPSOB-0.3 SE is superior to that of NCM-811 in liquid electrolyte [66]. The use of SE provides a promising way to achieve high performance and high safety Ni-rich NCM-based LIBs.

To further understand the excellent electrochemical performance of the cell with LPSOB-0.3 electrolyte, EIS analysis (Fig. 5c) was carried out on the full cells before and after charging. The resistance of LPSOB-0.3 cell is slightly lower than that of LPSB cell before cycling, whereas the difference of the resistance becomes significantly enlarged after charging to 3.7 V. This again confirms that incorporation of oxygen decreases the side reaction at the interfaces of SE/electrodes. A comprehensive improvement (Fig. 6) is achieved via O doping on LPSB argyrodite SEs.

The repeatability of all-solid-state NCM-811/Li—In batteries (Fig. S13) with LPSOB-0.3 and LPSB SEs were respectively tested for 3 times. Different batches show similar data, indicating well repeatable results. The cells using LPSOB-0.3 achieve higher theoretical capacity than that using LPSB, corroborating the superiority of O doping in LPSB SE.

The similar results are also seen from all-solid-state batteries based on $LiCoO_2$ cathode (Fig. S14), i.e., the cell using LPSOB-0.3 SE achieves better interfacial stability and rate capability, as well as higher capacity than that using LPSB. Oxygen incorporation on sulfide SEs would be an universal strategy to improve the electrochemical performance for all-solid-state batteries.

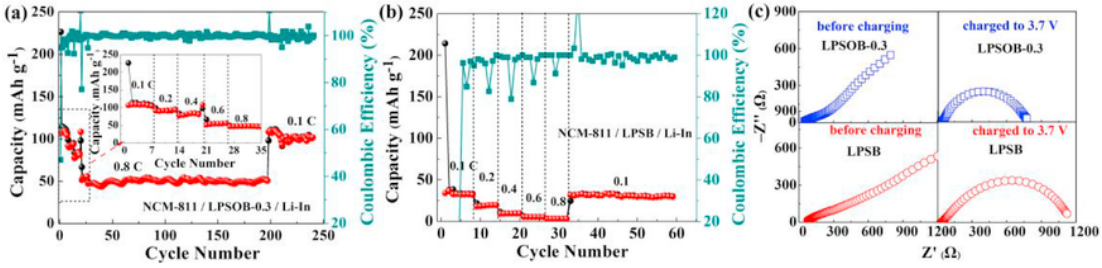

Fig. 5. Cycling and rate performance of the NCM-811/Li—In cells with the electrolyte of (a) LPSOB-0.3 and (b) LPSB. (c) Impedance spectra of the NCM-811/Li—In cells using the electrolyte of LPSOB-0.3 and LPSB before charging and after charging to 3.7 V *versus* Li—In.

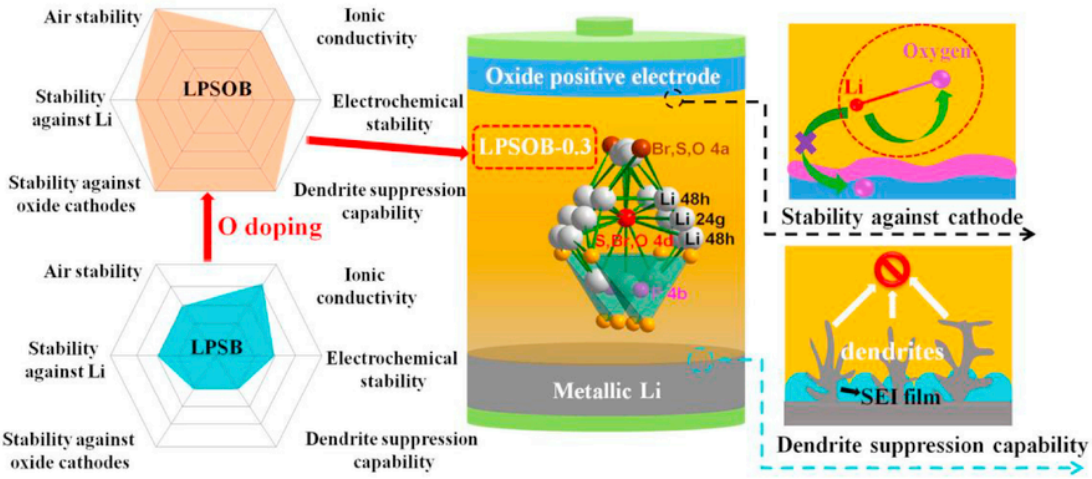

Fig. 6. Schematic illustration depicting the superiority of O-doped electrolyte and all-solid-state battery with this SE.

4. Conclusion

The argyrodite $Li_6PS_{5-x}O_xBr$ ($0 \leq x \leq 1$) SEs were synthesized by solid-state sintering, investigated systematically for the electrochemical properties, and tested in all-solid-state batteries with NCM-811 and Li-CoO_2 cathode. Combined the analysis of DFT calculation and Raman spectra, O atoms were found to prefer to substitute S atoms at the 4*a* and/or 4*d* sites rather than the 16*e* site. A moderate O concentration does not affect the ionic conductivity of $Li_6PS_{5-x}O_xBr$ even if formed little impurities. Undoubtedly, O-doped samples demonstrate improved air stability. More important, observed from galvanostatic intermittent cycling tests with step-increased current density and ex situ SEM, O incorporation intensively enhances Li dendrite suppression capability of the SEs. The CV and EIS measurements reveal respectively that O-doped electrolyte achieves much better electrochemical and chemical stability against metallic Li than O-free electrolyte. Molten Li intensively reacts with O-free LPSB. In parallel, O doping improves the compatibility of oxide cathode/electrolyte with a reduced interfacial resistance. Given these superiorities of O-doped LPSB, all-solid-state cells with this electrolyte achieve higher capacity and better rate capability than O-free electrolyte. What is more, using Li metal as negative electrode, NCM-811 cell reaches stable cycling over 92 cycles with LPSOB-0.3 SEs but fails at 2nd charging process with LPSB SEs. Further considering the excellent cycling stability, $Li_6PS_{5-x}O_xBr$ is thus one of the very promising SEs for ASLIBs.

Competing financial interest

The authors declare no competing financial interest.

Acknowledgements

This work was supported by the National Key R&D Program of China (Grant No. 2018YFB0104300), the Natural Science Foundation of Hebei Province (E2018203301), and the Science Foundation of Hebei Education Department (ZD2016033).

Appendix A. Supplementary data

Supplementary data to this article can be found online at https://doi.org/10.1016/j.jpowsour.2018.11.016.

References

[1] K.H. Park, Q. Bai, D.H. Kim, D.Y. Oh, Y. Zhu, Y. Mo, Y.S. Jung, Adv. Energy Mater. 8 (2018), 1800035.
[2] A. Manthiram, X. Yu, S. Wang, Nat. Rev. Mater. 2 (2017), 16103.
[3] J.C. Bachman, S. Muy, A. Grimaud, H.-H. Chang, N. Pour, S.F. Lux, O. Paschos, F. Maglia, S. Lupart, P. Lamp, L. Giordano, Y. Shao-Horn, Chem. Rev. 116 (2016) 140–162.
[4] K. Takada, T. Ohno, N. Ohta, T. Ohnishi, Y. Tanaka, ACS Energy Lett 3 (2017) 98–103.
[5] S.P. Culver, R. Koerver, T. Krauskopf, W.G. Zeier, Chem. Mater. 30 (2018) 4179–4192.
[6] J. Yue, M. Yan, Y.-X. Yin, Y.-G. Guo, Adv. Funct. Mater. 28 (2018), 1707533.
[7] B. Zheng, H. Wang, J. Ma, Z. Gong, Y. Yang, Sci. Sin. Chim. 47 (2017) 579–593.
[8] W.D. Richards, L.J. Miara, Y. Wang, J.C. Kim, G. Ceder, Chem. Mater. 28 (2016) 266–273.
[9] J. Ma, B. Chen, L. Wang, G. Cui, J. Power Sources 392 (2018) 94–115.
[10] S. Chen, D. Xie, G. Liu, J.P. Mwizerwa, Q. Zhang, Y. Zhao, X. Xu, X. Yao, Energy Storage Mater 14 (2018) 58–74.
[11] L. Fan, S. Wei, S. Li, Q. Li, Y. Lu, Adv. Energy Mater. 8 (2018), 1702657.
[12] A. Hayashi, A. Sakuda, M. Tatsumisago, Front. Energy Res. 4 (2016) 25.
[13] F. Zheng, M. Kotobuki, S. Song, M.O. Lai, L. Lu, J. Power Sources 389 (2018) 198–213.
[14] Z. Zhang, L. Zhang, Y. Liu, C. Yu, X. Yan, B. Xu, L.-m. Wang, J. Alloy. Comp. 747 (2018) 227–235.
[15] C. Yu, S. Ganapathy, N.J. de Klerk, I. Roslon, E.R. van Eck, A.P. Kentgens, M. Wagemaker, J. Am. Chem. Soc. 138 (2016) 11192–11201.
[16] S. Chida, A. Miura, N.C. Rosero-Navarro, M. Higuchi, N.H.H. Phuc, H. Muto, A. Matsuda, K. Tadanaga, Ceram. Int. 44 (2018) 742–746.
[17] S. Yubuchi, S. Teragawa, K. Aso, K. Tadanaga, A. Hayashi, M. Tatsumisago, J. Power Sources 293 (2015) 941–945.
[18] H.J. Deiseroth, S.T. Kong, H. Eckert, J. Vannahme, C. Reiner, T. Zaiss, M. Schlosser, Angew. Chem. 47 (2008) 755–758.
[19] Y. Zhu, X. He, Y. Mo, ACS Appl. Mater. Interfaces 7 (2015) 23685–23693.
[20] J. Auvergniot, A. Cassel, J.-B. Ledeuil, V. Viallet, V. Seznec, R. Dedryvère, Chem. Mater. 29 (2017) 3883–3890.
[21] J. Auvergniot, A. Cassel, D. Foix, V. Viallet, V. Seznec, R. Dedryvère, Solid State Ionics 300 (2017) 78–85.
[22] J. Maier, Prog. Solid State Chem. 23 (1995) 171–263.
[23] K. Takada, N. Ohta, L. Zhang, X. Xu, B.T. Hang, T. Ohnishi, M. Osada, T. Sasaki, Solid State Ionics 225 (2012) 594–597.
[24] M. Haruta, S. Shiraki, T. Suzuki, A. Kumatani, T. Ohsawa, Y. Takagi, R. Shimizu, T. Hitosugi, Nano Lett. 15 (2015) 1498–1502.
[25] K.H. Kim, Y. Iriyama, K. Yamamoto, S. Kumazaki, T. Asaka, K. Tanabe, C.A.J. Fisher, T. Hirayama, R. Murugan, Z. Ogumi, J. Power Sources 196 (2011) 764–767.
[26] A. Sakuda, A. Hayashi, M. Tatsumisago, Chem. Mater. 22 (2010) 949–956.
[27] S. Wenzel, S.J. Sedlmaier, C. Dietrich, W.G. Zeier, J. Janek, Solid State Ionics 318 (2018) 102–112.
[28] C. Yu, L. van Eijck, S. Ganapathy, M. Wagemaker, Electrochim. Acta 215 (2016) 93–99.
[29] F. Han, J. Yue, X. Zhu, C. Wang, Adv. Energy Mater. 8 (2018), 1703644.
[30] R. Garcia-Mendez, F. Mizuno, R. Zhang, T.S. Arthur, J. Sakamoto, Electrochim. Acta 237 (2017) 144–151.
[31] S. Ujiie, A. Hayashi, M. Tatsumisago, Solid State Ionics 211 (2012) 42–45.

[32] S. Ujiie, A. Hayashi, M. Tatsumisago, J. Solid State Electrochem. 17 (2012) 675–680.
[33] T. Ohtomo, A. Hayashi, M. Tatsumisago, K. Kawamoto, J. Solid State Electrochem. 17 (2013) 2551–2557.
[34] Y. Sun, K. Suzuki, K. Hara, S. Hori, T.-a. Yano, M. Hara, M. Hirayama, R. Kanno, J. Power Sources 324 (2016) 798–803.
[35] Y. Tao, S. Chen, D. Liu, G. Peng, X. Yao, X. Xu, J. Electrochem. Soc. 163 (2016) A96–A101.
[36] B. Huang, X. Yao, Z. Huang, Y. Guan, Y. Jin, X. Xu, J. Power Sources 284 (2015) 206–211.
[37] X. Wang, R. Xiao, H. Li, L. Chen, Phys. Rev. Lett. 118 (2017), 195901.
[38] K. Suzuki, M. Sakuma, S. Hori, T. Nakazawa, M. Nagao, M. Yonemura, M. Hirayama, R. Kanno, Solid State Ionics 288 (2016) 229–234.
[39] A. Makishima, J.D. Mackenzie, J. Non-Cryst. Solids 12 (1973) 35–45.
[40] A. Kato, M. Nagao, A. Sakuda, A. Hayashi, M. Tatsumisago, J. Ceram. Soc. Jpn. 122 (2014) 552–555.
[41] N.D. Lepley, N.A.W. Holzwarth, Y.A. Du, Phys. Rev. B 88 (2013), 104103.
[42] T. Ohtomo, A. Hayashi, M. Tatsumisago, K. Kawamoto, J. Non-Cryst. Solids 364 (2013) 57–61.
[43] F. Mizuno, A. Hayashi, K. Tadanaga, M. Tatsumisago, J. Electrochem. Soc. 152 (2005) A1499–A1503.
[44] Y. Kato, S. Hori, T. Saito, K. Suzuki, M. Hirayama, A. Mitsui, M. Yonemura, H. Iba, R. Kanno, Nat. Energy 1 (2016), 16030.
[45] J. Rodriguez-Carvajal, Phys. B 192 (1993) 55–69.
[46] I.P. Studenyak, V.O. Stefanovich, M. Kranjčec, D.I. Desnica, Y.M. Azhnyuk, G.S. Kovacs, V.V. Panko, Solid State Ionics 95 (1997) 221–225.
[47] R.V. Gorbachev, I. Riaz, R.R. Nair, R. Jalil, L. Britnell, B.D. Belle, E.W. Hill, K.S. Novoselov, K. Watanabe, T. Taniguchi, A.K. Geim, P. Blake, Small 7 (2011) 465–468.
[48] T. Ohtomo, A. Hayashi, M. Tatsumisago, K. Kawamoto, Electrochemistry 81 (2013) 428–431.
[49] O. Takamasa, K. Koji, H. Masahiro, Cancum, Mexico, 2012.
[50] C. Yang, K. Fu, Y. Zhang, E. Hitz, L. Hu, Adv. Mater. 29 (2017), 1701169.
[51] C. Monroe, J. Newman, J. Electrochem. Soc. 152 (2005) A396–A404.
[52] Z. Deng, Z. Wang, I.-H. Chu, J. Luo, S.P. Ong, J. Electrochem. Soc. 163 (2015) A67–A74.
[53] S. Li, J. Zhu, Y. Wang, J.W. Howard, X. Lü, Y. Li, R.S. Kumar, L. Wang, L.L. Daemen, Y. Zhao, Solid State Ionics 284 (2016) 14–19.
[54] N.W. Li, Y.X. Yin, C.P. Yang, Y.G. Guo, Adv. Mater. 28 (2016) 1853–1858.
[55] S.-T. Kong, H.-J. Deiseroth, J. Maier, V. Nickel, K. Weichert, C. Reiner, Z. Anorg. Allg. Chem. 636 (2010) 1920–1924.
[56] P.R. Rayavarapu, N. Sharma, V.K. Peterson, S. Adams, J. Solid State Electrochem. 16 (2011) 1807–1813.
[57] K. Minami, A. Hayashi, S. Ujiie, M. Tatsumisago, Solid State Ionics 192 (2011) 122–125.
[58] K. Minami, A. Hayashi, M. Tatsumisago, Solid State Ionics 179 (2008) 1282–1285.
[59] I.S. Kang, Y.S. Lee, D.W. Kim, J. Electrochem. Soc. 161 (2013) A53–A57.
[60] S. Wenzel, S. Randau, T. Leichtweiß, D.A. Weber, J. Sann, W.G. Zeier, J. Janek, Chem. Mater. 28 (2016) 2400–2407.
[61] S. Wenzel, D.A. Weber, T. Leichtweiss, M.R. Busche, J. Sann, J. Janek, Solid State Ionics 286 (2016) 24–33.
[62] T. Kazunori, A. Noboru, I. Kazuya, K. Shigeo, Solid State Ionics 86 (1996) 877–882.
[63] J.E. Trevey, J.R. Gilsdorf, S.W. Miller, S.-H. Lee, Solid State Ionics 214 (2012) 25–30.
[64] R. Koerver, I. Aygün, T. Leichtweiß, C. Dietrich, W. Zhang, J.O. Binder, P. Hartmann, W.G. Zeier, J. Janek, Chem. Mater. 29 (2017) 5574–5582.
[65] K. Takada, N. Ohta, L. Zhang, K. Fukuda, I. Sakaguchi, R. Ma, M. Osada, T. Sasaki, Solid State Ionics 179 (2008) 1333–1337.
[66] B.-J. Chae, T. Yim, J. Power Sources 360 (2017) 480–487.